

## A Simple Model of Climatological Rainfall and Vertical Motion Patterns over the Tropical Oceans

LARISSA E. BACK

*Department of Earth, Atmospheric, and Planetary Sciences, Massachusetts Institute of Technology, Cambridge, Massachusetts*

CHRISTOPHER S. BREThERTON

*Department of Atmospheric Sciences, University of Washington, Seattle, Washington*

(Manuscript received 20 December 2007, in final form 3 June 2009)

### ABSTRACT

A simple model is developed that predicts climatological rainfall, vertical motion, and diabatic heating profiles over the tropical oceans given the sea surface temperature (SST), using statistical relationships deduced from the 40-yr ECMWF Re-Analysis (ERA-40). The model allows for two modes of variability in the vertical motion profiles: a shallow mode responsible for all “boundary layer” convergence between 850 hPa and the surface, and a deep mode with no boundary layer convergence. The model is based on the argument expressed in the authors’ companion paper that boundary layer convergence can be usefully viewed as a forcing on deep convection, not just a result thereof. The shallow mode is either specified from satellite observations or modeled using a simple mixed-layer model that has SST as well as 850-hPa geopotential height, winds, and temperature as boundary conditions. The deep-mode amplitude is empirically shown to be proportional to a simple measure of conditional instability in convecting regions, and is determined by the constraint that radiative cooling must balance adiabatic warming in subsidence regions.

This two-mode model is tested against a reanalysis-derived dry static energy budget and in a reanalysis-independent framework based on satellite-derived surface convergence and using SST as a proxy for conditional instability. It can predict the observed annual mean and seasonal cycle of rainfall, vertical motion, and diabatic heating profiles across the tropical oceans with significantly more skill than optimized predictions using a thresholded linear relationship with SST. In most warm-ocean regions, significant rainfall only occurs in regions of monthly-mean boundary layer convergence. In such regions, deep-mode amplitude and rainfall increase linearly with SST, with an additional rainfall contribution from the shallow mode directly tied to boundary layer convergence. This second contribution is significant mainly in the east and central Pacific ITCZ, where it is responsible for that region’s “bottom-heavy” vertical-velocity, diabatic heating, and cloud profiles.

### 1. Introduction

In the tropics, deep convection strongly influences the large-scale atmospheric circulation (e.g., Matsuno 1966; Gill 1980). As has also been known for some time, the distribution of sea surface temperature (SST) has a strong effect on deep convection (e.g., Bjerknes 1969; Webster 1981; Zebiak 1982). Hence, understanding how climatological rainfall and latent heating patterns relate to the observed SST distribution is an essential component of

any conceptual model or simple theory of the large-scale tropical circulation. Simple models can also give valuable intuitive understanding of what may be occurring in more complex simulations and parameterizations that are less easily understood from first principles. In this work, using a combination of physical reasoning and empiricism, we develop a simple model that predicts monthly rainfall and vertical motion profiles from SST and surface convergence with skill comparable to current atmospheric general circulation models (AGCMs). Our model also predicts the vertical distribution of the diabatic heating associated with this convection, which has also been shown to substantially affect the large-scale circulation (Hartmann et al. 1984; Wu et al. 2000; Schumacher et al. 2004; Back and Bretherton 2006).

---

*Corresponding author address:* Larissa Back, Department of Earth, Atmospheric, and Planetary Sciences, Massachusetts Institute of Technology, Building 54-1624, 77 Massachusetts Ave., Cambridge, MA 02139.  
E-mail: lback@mit.edu

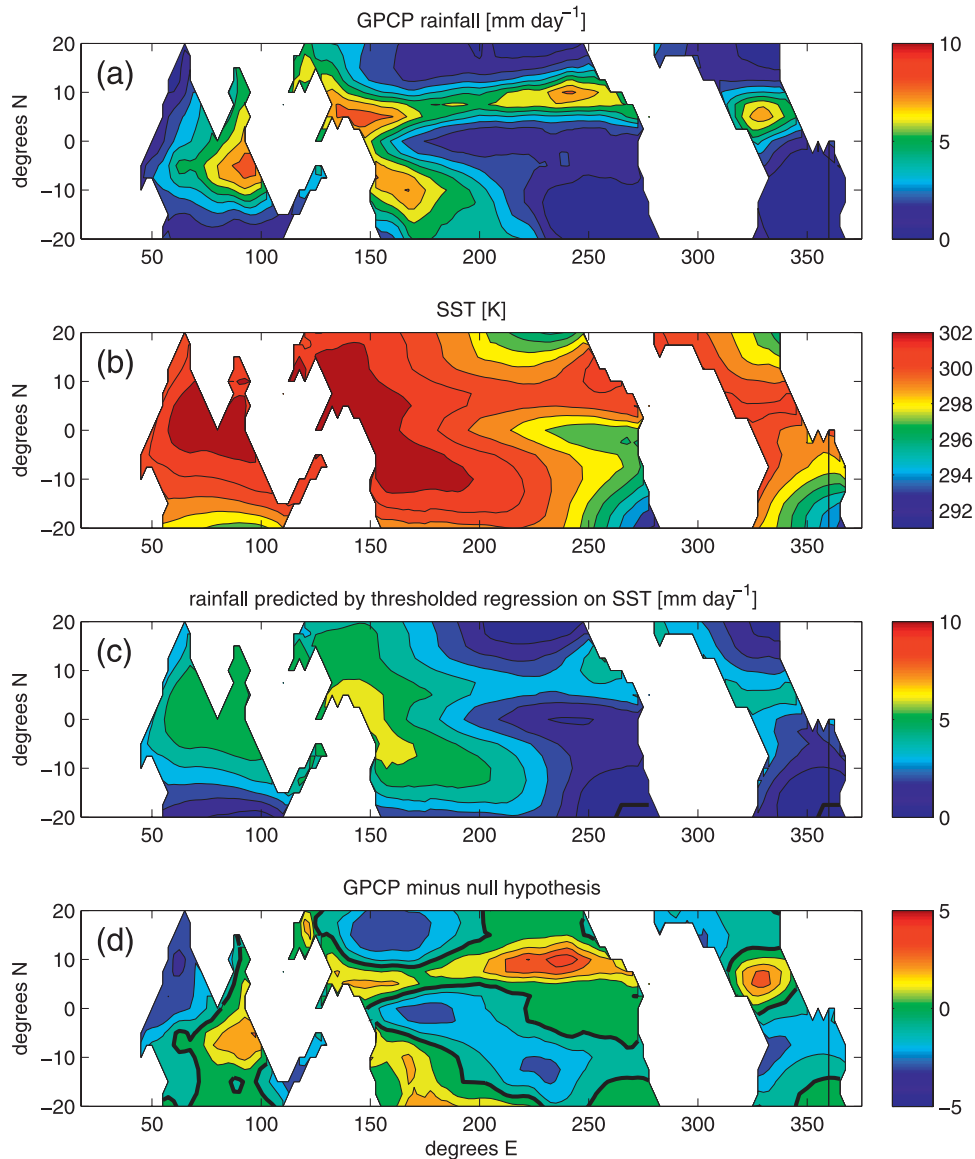


FIG. 1. Time-averaged 1998–2001: (a) GPCP precipitation, (b) SST, (c) null hypothesis precipitation [regression on SST using (1)], and (d) GPCP precipitation minus null hypothesis precipitation.

To a first approximation, deep convection occurs over the warmest SSTs, as can be seen in the rainfall and SST climatologies shown in Figs. 1a,b. This can be rationalized from the local column thermodynamics as follows: free-tropospheric temperature varies much less than SST in the tropics, so conditional instability and convective available potential energy (CAPE) are largest over the warmest SST. The relationship is known to be imperfect (e.g., Ramage 1977; Zhang 1993; Fu et al. 1994; Bony et al. 1997), but has been quite influential, and is a key assumption of many simple models (e.g., Webster 1981; Zebiak 1982, 1986; Neelin and Held 1987), so we quantify it using a “null hypothesis” model

that predicts monthly-mean rainfall over the tropical oceans purely as a linear function of monthly SST (above a threshold):

$$P(x, y, t) = a_0 [T_s(x, y, t) - b_0] H[T_s(x, y, t) - b_0], \quad (1)$$

where the Heaviside function is denoted  $H$  and  $T_s$  is monthly SST. The constants  $a_0 = 1.3 \text{ mm day}^{-1} \text{ K}^{-1}$  and  $b_0 = 298 \text{ K}$  have been tuned via a nonlinear optimization procedure (MATLAB function “fminsearch”; algorithm is described in Lagarias et al. 1998) to minimize the root-mean-square error in the predicted time-mean rainfall compared to satellite observations from the

TABLE 1. Spatial correlation coefficients ( $r$ ) of rainfall over ocean grid points in 20°S–20°N (cf. GPCP) for models discussed in this paper. The null hypothesis model (thresholded regression on SST) is denoted by h0. The AGCM column shows the range of values for three AGCM climatologies described in Back and Bretherton (2009). Seasonal space–time correlations are based on 1998–2001 seasonal anomalies (DJF, MAM, JJA, and SON) with respect to the predicted or observed mean state (for qSCAT where 2000–01 data was used instead of 1998–2001).

$r$	h0	qSCAT	MLM	MLM-SST	AGCMs
Annual mean	0.77	0.92	0.82	0.79	0.83–0.90
Seasonal anomalies	0.61	0.77	0.72	0.65	NA

Global Precipitation Climatology Project (GPCP; Adler et al. 2003)]. In this model, SST gradients and the boundary layer winds do not enter the rainfall prediction. We quantify the skill of the null hypothesis model in terms of the spatial correlation coefficient  $r = 0.77$  of its annual-mean rainfall with GPCP, and a time–space correlation coefficient  $r = 0.61$  of seasonal rainfall anomalies from this mean. These correlation coefficients, shown in the first column of Table 1, provide a baseline for evaluating other simple models, including the two-mode empirical models we develop in this work.

Figure 1c shows the null hypothesis model annual-mean precipitation distribution. It shares many features of the observed (GPCP) precipitation field. However, a difference map (Fig. 1d) shows that the observed ITCZs are narrower and more intense than SST alone would imply. The differences are particularly pronounced in the central-eastern Pacific and Atlantic ITCZs, where observed ITCZs are narrow. This is particularly notable since based on thermodynamic reasoning alone, one might expect the null hypothesis model to overestimate rainfall in regions with narrow ITCZs and strong SST gradients, because of more advection of dry air into narrower ITCZs. Surface convergence (e.g., Back and Bretherton 2009, hereafter BB09; see their Fig. 1a) is strong in many of the regions where the null hypothesis model underpredicts rainfall (this is also clear from Fu et al. 1994), and occurs in narrower bands than the SST maxima. This suggests that surface convergence (at least the component that is not due to deep convection) may be a useful supplement to SST for explaining the rainfall distribution.

Implicit in the null hypothesis model as well as simple models based on the column-integrated moist static energy budget (e.g., Neelin and Held 1987; Neelin and Zeng 2000) is the assumption that deep convection induces the lower-tropospheric convergence required to maintain a sufficient moisture supply for further convection. An alternative view, broadly supported by the results of our companion paper (BB09), which was proposed by Lindzen and Nigam (1987, hereafter

LN87), who designed a simple model of the zonally asymmetric circulation and convergence distribution from SST. In the LN87 model, SST gradients imprint on the temperature of the shallow cumulus boundary layer, which leads to surface pressure gradients and frictional convergence. LN87 argue this convergence causes deep convection, in contrast to the null hypothesis model in which boundary layer convergence is a consequence of deep convection.

While the LN87 mechanism is physically distinct from the convection-induced convergence mechanism, the relative roles of the two mechanisms in causing the rainfall observed in nature has been unclear and the relationship between these views has been subject to some debate (Neelin 1989; Wang and Li 1993; Battisti et al. 1999; Sobel and Neelin 2006; Sobel 2007). This issue has complicated the physical interpretation of theoretically based models, as well as empirical relationships between SST, surface convergence, and rainfall (Sobel 2007 reviews these issues in more detail). Better understanding of this question is a major motivation for the simple rainfall model we develop, as well as for the work described in our companion paper (BB09).

In BB09, we diagnosed the forcing of observed surface and boundary layer (surface to 850 hPa) convergence. We found that across the tropical oceans, 850-hPa winds, and geopotential height gradients, which are partially a consequence of the distribution of deep convection, have only a small influence on surface convergence patterns. Instead, surface convergence patterns and 850-hPa vertical motion are predominantly due to SST gradients imprinting on the boundary layer, causing surface pressure gradients and frictional convergence. Hence, at least in our present climate, surface convergence can usefully be viewed as predominantly a cause rather than a consequence of the distribution of deep convection. However, BB09 also noted that to quantitatively model surface convergence, it is important to include the contribution of 850-hPa winds, temperature, and geopotential height, showing that free-tropospheric heating may affect surface convergence. (The present two-mode model deliberately treats this effect as an external forcing on the surface convergence, because its accurate prediction would require a crude prediction of the mean tropical circulation driven by the entire global distribution of diabatic heating, including over land. While this is essential for a full model of tropical rainfall distribution, it adds complexity that would obscure our present purpose of showing that a two-mode model can capture the main features of this distribution). The BB09 results broadly support LN87's idea that most boundary layer convergence is due to SST gradients, though BB09 diverged substantially from the

LN87 model of how free-tropospheric processes can affect boundary layer convergence.

An issue that was not addressed by LN87 or our companion paper is how boundary layer convergence is related to rainfall and latent heating. While surface convergence [i.e., Quick Scatterometer (QuikSCAT)] and rainfall (i.e., GPCP) are strongly correlated ( $r = 0.75$ ), the distribution of surface convergence alone cannot explain a number of important features of the rainfall distribution. For example, over the northwestern Pacific warm pool, maximum convergence is less than half the maximum convergence in the eastern Pacific, though rainfall maxima in both cases are  $9 \text{ mm day}^{-1}$ . The simple rainfall model we develop in this work is based on the hypothesis that variations in the amount of rainfall per unit surface convergence are due to differences in instability in these regions consistent with the analysis of Fu et al. (1994); Wang and Li (1993).

Another important aspect of rainfall distribution that motivates our model is the observed geographic variability in vertical motion profiles (Trenberth et al. 2000; Zhang et al. 2004a; Back and Bretherton 2006) and closely related quantities like latent heating (Chan and Nigam 2009), cloud-top heights (Kubar et al. 2007; Mote and Frey 2006), and cloud-radiative forcing (Bretherton and Hartmann 2008). Large-scale vertical motion profiles in the central-eastern Pacific ITCZ are “bottom heavy” with strong boundary layer horizontal convergence, maximum vertical motion around 850 hPa, and horizontal divergence above, implying a negative “gross moist stability” (Back and Bretherton 2006). In contrast, over the western Pacific, boundary layer convergence is weak and mean horizontal convergence extends to above 400 hPa. Since previous literature has documented the substantial effects of variations in the vertical profile of diabatic heating on the large-scale circulation (Hartmann et al. 1984; Wu et al. 2000; Schumacher et al. 2004), the goal of retrieving vertical profiles of latent heating from satellite data has driven the development of a number of algorithms for processing data from the Tropical Rainfall Measuring Mission (TRMM; Tao et al. 2006). Our simple rainfall model illuminates some of the large-scale constraints that influence these vertical motion and diabatic heating profiles on climatological time scales.

Past theoretical work on the climatological distribution of deep convection has generally assumed only one geographically invariant mode of vertical motion variability or heating associated with deep convection (Gill 1980; Zebiak 1986; Neelin and Zeng 2000). This also roughly corresponds to assuming a linear relationship between surface convergence and rainfall in precipitating regions. Since observationally based studies (such as those mentioned above) have shown that this simplifying assumption

is ill founded, and we are interested in exploring extensions to this view, in our model we use two empirically derived modes of variability in vertical motion, which also allows for a nonlinear relationship between surface convergence and rainfall. This is important to our methodology, and makes it possible to include contributions from both the LN87 mechanism and the convection-induced convergence mechanism in our model of the rainfall distribution.

In this work, we use SST and surface convergence as predictors in a simple model for understanding the geographical variability in vertical motion, latent heating, and radiative cooling profiles on monthly and longer time scales. The model predicts the amplitude of a shallow, convergence-driven mode, and a deep, instability-driven mode of vertical motion, and rainfall is derived from the amplitude of these modes using the dry static energy budget. For this purpose, we first use the observed surface convergence pattern, then we predict the convergence using BB09’s simple boundary layer convergence model (based on the surface wind model of Stevens et al. 2002). Cloud-radiative effects are internally determined from the two modes based on empirical linear regression.

The data we use for our analysis is described in section 2. Section 3 describes the procedure we use to obtain two vertical basis functions that describe variability in vertical motion profiles and the relationship between surface convergence and rainfall. In section 4, we describe statistical relationships showing that vertical motion profiles in the 40-yr European Centre for Medium-Range Weather Forecasts (ECMWF) Re-Analysis (ERA-40) are related to a measure of conditional instability, which is closely correlated with SST. We use the results of this analysis to develop the rainfall and vertical motion profile model that uses SST and boundary layer convergence as inputs. The approach developed from ERA-40 is tested in a reanalysis-independent framework in section 6, in which we use observed SST and surface convergence patterns to predict the annual mean and seasonal anomalies of rainfall with considerably more skill than the null hypothesis model based on SST alone.

In section 5, we discuss why we were not able to use the column-integrated moist static energy budget to determine the deep-mode amplitude, an approach suggested by previous theoretical studies (Neelin and Held 1987; Neelin and Zeng 2000; Sobel and Neelin 2006). Readers unfamiliar with or uninterested in this approach can skip over this section.

We combine BB09’s mixed-layer model framework (based on Stevens et al. 2002) for predicting surface convergence with our approach for predicting rainfall and vertical motion profiles in section 7. In this model, 850-hPa temperature, pressure gradients, and horizontal

winds (which respond to the global-scale distribution of tropical deep convection) are taken as boundary conditions in addition to SST. The skill of the resulting rainfall and vertical motion predictions are compared with the observed-convergence model. Section 8 contains the conclusions and a discussion of the implications of our results.

## 2. Data description

From the data support section of the National Center for Atmospheric Research (NCAR), we obtained monthly, 1998–2001 ERA-40 (23 pressure levels, 2.5° grid; Uppala et al. 2005) temperature, wind speeds, humidity, surface latent and sensible heat fluxes, and radiative fluxes at the surface and top of atmosphere. This data was used to choose vertical modes and relate these to the rainfall and vertical motion distribution via the column-integrated dry static energy ( $s$ ) budget. Throughout the analysis, we only use monthly data from ocean points as defined by ERA-40, and restrict analysis to latitudes less than or equal to 20° from the equator. We also use data from a second reanalysis, the (National Centers for Environmental Prediction) NCEP–NCAR reanalysis to check our results (Kalnay et al. 1996).

As described in our companion paper (Back and Bretherton 2009), via Remote Sensing Systems, we also obtained 2000–01 data from the National Aeronautics and Space Administration (NASA) SeaWinds instrument on QuikSCAT, and computed monthly averaged surface wind and convergence fields averaged to 2.5° resolution (shown in Fig. 1a of BB09). We also utilized GPCP rainfall estimates interpolated to the ERA-40 grid, as well as satellite-derived surface and top-of-atmosphere (TOA) radiative flux estimates from the International Satellite Cloud Climatology Project (ISCCP; Zhang et al. 2004b), which we obtained from their Web site (<http://isccp.giss.nasa.gov>).

## 3. Modal decomposition of vertical motion profiles

Two vertical modes are necessary to represent observed variations in the height of maximum vertical motion and corresponding variations in the relationship between BL convergence and rainfall. We choose basis vectors that we use to define our modes by performing a principal component analysis (PCA) on ERA-40 monthly horizontal convergence profiles over the tropical oceans (20°S–20°N, 1998–2001) to extract the two dominant vertical modes of space–time variability. The first of the PCA modes, shown by the thick solid line in Fig. 2a, explains 56% of the overall variance in the convergence profiles and reflects the correlation between surface

convergence and vertical motion noted in Fig. 1. The second PCA mode, shown by the thick dashed line in Fig. 2 explains 14% of the variance (the third mode explains 9% of the variance). Over 80 000 profiles were used in the PCA, and the extremely conservative choice of 40 degrees of freedom leads a +2%–95% confidence interval on the second PCA mode (by North et al. 1982, criterion), so the second PCA is very significant. This second PCA mode is associated with variations in bottom heaviness of vertical motion profiles, but is not strongly correlated with the amount of rainfall. The mean convergence over the tropical oceans is small compared with the geographic variability of the PCA modes.

Throughout Fig. 2, comparable modes of variability obtained using the NCEP reanalysis are shown in thin lines. In NCEP, the first 3 PCA modes explain 54%, 14%, and 8% of the variance, respectively, so, as in ERA-40, the second mode is highly significant.

Figure 2b shows the vertical motion profiles associated with these PCA modes, computed by integrating the horizontal convergence downward from 100 hPa where vertical motion is assumed to be zero. Horizontal convergence from the lowest layer is extrapolated to the mean surface pressure and residual convergence required for vertical motion profiles to satisfy mass continuity is uniformly distributed between the surface and 100 hPa. The nature of our results is not sensitive to this assumption. These vertical motion profiles explain more than 92% of the variance in vertical motion in ERA-40 (91% in NCEP).

The PCA modes shown in Figs. 2a,b both involve variability in boundary layer convergence. Any orthogonal linear combination of these modes provides an equally accurate basis for describing the ERA-40 convergence and vertical motion. To separate variability associated with boundary layer convergence from other variability in vertical motion profiles, we linearly combine the dominant modes of variability such that only one mode projects on the near-surface (below 925 hPa) convergence, and the two resulting modes have orthogonal divergence profiles.

The horizontal convergence profiles and associated vertical motion profiles from this procedure are shown in Figs. 2c,d. Hereafter, the mode that projects strongly on surface convergence will be referred to as the shallow mode, while the mode that has no horizontal convergence below 925 hPa will be referred to as the deep mode.

Figures 2e,f show maps of the fraction of the “local” variance explained by these two modes, where local variance is computed with respect to the tropical mean profile. The shallow mode explains the most variance in the central-eastern Pacific ITCZ and Atlantic, while the deep mode explains more variance other rainy regions.

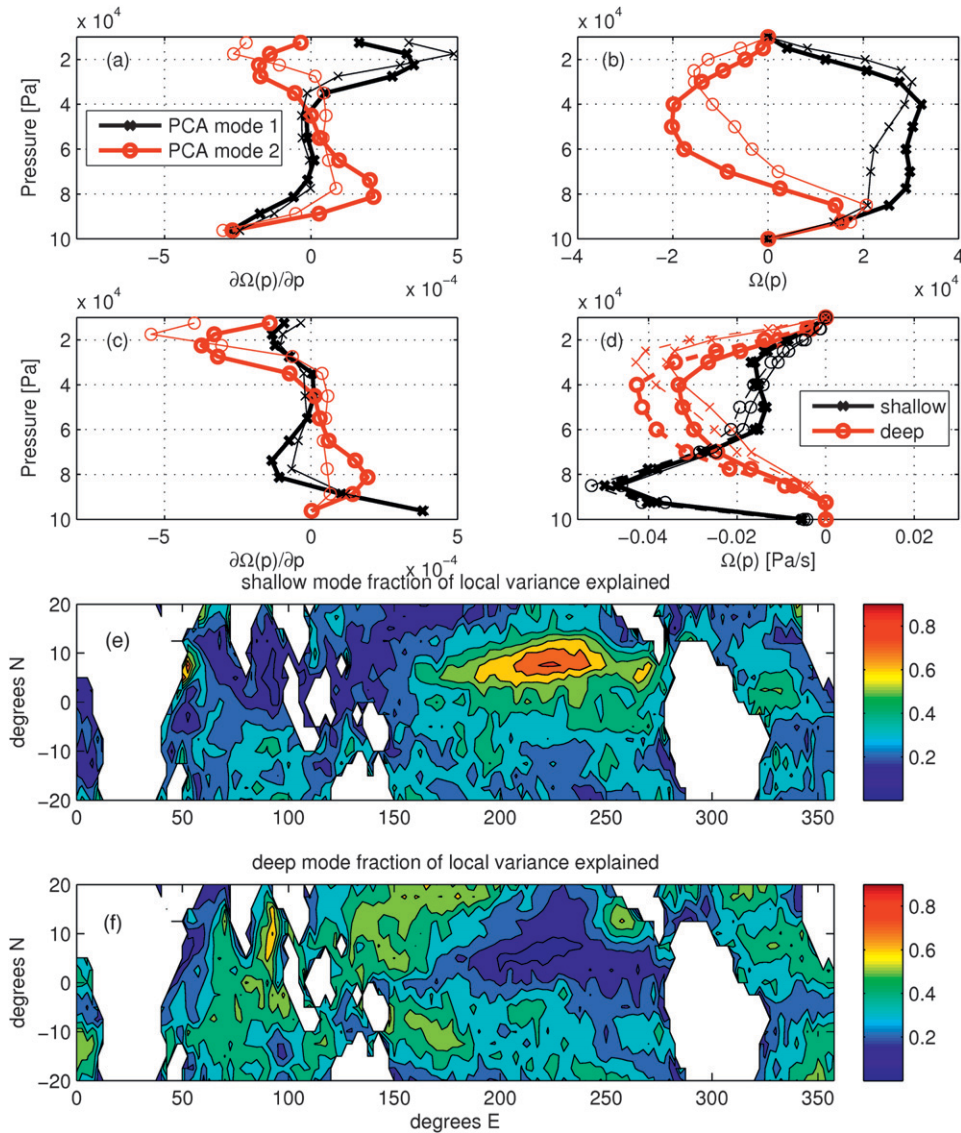


FIG. 2. (a)–(d) Empirically derived horizontal convergence and vertical motion modes from ERA-40 (thick lines) and NCEP (thin lines). (a),(c) Horizontal convergence profiles; (b),(d) corresponding vertical motion profiles. (a),(b) Modes as estimated PCA of horizontal convergence; (c),(d) the linear combinations of these modes used in subsequent analysis. Scaling arbitrary except in (d) where vertical motion normalized to profile associated with  $100 \text{ W m}^{-2}$  diabatic heating: solid lines do not include cloud-radiative forcing changes in normalization, but dashed lines do. (e),(f) Fraction of “local” convergence variance (w.r.t. tropical mean) explained by the shallow and deep mode. The contour interval is 0.1.

An alternative choice of basis modes (which gives similar results) would be specify the deep mode as contributing no horizontal convergence below 850 hPa. We choose 925 hPa because in ERA-40, vertical motion at the 925-hPa level is slightly better correlated with surface convergence in ERA-40 than is 850-hPa vertical motion ( $r = 0.93$  versus  $r = 0.88$ ), and so some of the variations in the relationship between surface convergence and 850-hPa vertical motion (discussed in our companion paper) are likely associated with deep-mode variability.

Describing vertical motion solely in terms of these two modes is equivalent to approximating large-scale vertical motion profiles,  $\omega(x, y, t, p)$  by the following truncation:

$$\omega(x, y, t, p) = o_1(x, y, t)\Omega_1(p) + o_2(x, y, t)\Omega_2(p), \quad (2)$$

where  $\Omega_1(p)$  is a vertical structure function describing the shape of the shallow mode, and  $\Omega_2(p)$  describes the vertical structure of the deep mode. The combination of large

(small) positive  $o_1$  and small (large)  $o_2$  correspond to more bottom-heavy (top heavy) upward motion profiles.

Previous work involving two-mode descriptions of vertical motion or latent heating profiles has used a variety of empirical and/or theoretical approaches to choosing the vertical modes (Moskowitz and Bretherton 2000; Trenberth et al. 2000; Mapes 2000; Majda and Shefter 2001; Schumacher et al. 2004; Peters and Bretherton 2006; Khouider and Majda 2006; Sobel and eelin 2006; Kuang 2008), which look broadly similar to orthogonal linear combinations of the modes we use in our analysis. In many of these studies, the modes have been described as convective and stratiform. However, since current observations suggest that variations in the ratio of stratiform rain fraction do not explain observed geographic variability in vertical motion profiles (Back and Bretherton 2006; Chan and Nigam 2009), we choose to describe our modes as shallow and deep instead.

#### a. Geographic distribution of modes in ERA-40

To quantitatively examine and model the contribution of the shallow- and deep-mode variability in vertical motion profiles to rainfall, we use the column-integrated budget of dry static energy,  $s = C_p T + gz$ . A similar budget is involved in the construction of simple tropical models based on the column-integrated moist static energy budget, and our notation follows these studies in some respects (Neelin and Zeng 2000; Yu et al. 1998).

The dominant balance in the  $s$  budget in the tropics over monthly and longer time scales is between adiabatic cooling associated with upward motion and apparent diabatic heating. Storage, horizontal  $s$  advection, and horizontal eddy flux convergence are weak over the tropical oceans because horizontal temperature gradients are small, especially above the boundary layer. Apparent diabatic heating variations (commonly defined as including diabatic heating as well as a typically small convergence of turbulent  $s$  fluxes; e.g., Yanai et al. 1973) are mainly due to latent heating, so rainfall variations are a large term in the column-integrated budget, and can be directly diagnosed from the adiabatic cooling (or vice versa) when equilibrium is assumed. Throughout our analysis, the geographic distribution of the two modes is expressed in terms of their contribution to the  $s$  budget to provide meaningful units for the amplitudes of these modes. The  $s$  budget also illustrates the constraints that a two vertical mode system with specified surface convergence must satisfy in a subsidence regime to avoid predicting negative rainfall.

We consider a tropospheric column extending from the surface to a nominal tropopause at 100 hPa. We assume that the monthly-mean pressure velocity is negligible at the surface and the tropopause, that monthly-mean  $s$

storage is negligible, that all precipitation reaches the surface as rain, that hydrometeor advection out of the column is negligible, that the heat capacity associated with water in all phases is negligible, and we apply the hydrostatic approximation. Then the column-integrated  $s$  conservation equation is

$$0 = -\left\langle u \frac{\partial s}{\partial x} + v \frac{\partial s}{\partial y} + \omega \frac{\partial s}{\partial p} \right\rangle + LP + \Delta F_{\text{rad}} + F_{\text{turb}}^s(0) + S_s, \quad (3)$$

where  $\langle \cdot \rangle$  indicates a mass-weighted integral over the column;  $u, v$  are horizontal winds;  $L$  is the latent heat of condensation;  $P$  is precipitation;  $\Delta F_{\text{rad}}$  is the net radiative flux convergence between the surface and 100 hPa;  $F_{\text{turb}}^s(0)$  is the surface sensible heat flux; and  $S_s$  is a residual. In the reanalysis calculations, the residual is mainly associated with the nonconservation of  $s$  in the forecast model due to nudging of the fields toward assimilated observations.

We calculate all terms in (3) from daily ERA-40 pressure-level data, assuming  $s$  is constant below 1000 hPa in the relatively well-mixed subcloud layer. As expected the dominant time-mean balance is between adiabatic cooling (warming) due to upward (downward) vertical motion, and diabatic warming (cooling) due to the sum of latent heating and radiative cooling in precipitating (non-precipitating) regions.

Because climatological horizontal temperature gradients and surface sensible heat fluxes over the tropical oceans are small, we neglect horizontal variations in  $s$  stratification, horizontal advection [first two terms on the right-hand side of Eq. (3)] and surface fluxes,  $F_{\text{turb}}^s(0)$ . Neglecting horizontal  $s$  advection and surface fluxes leads to a mean error of  $5 \text{ W m}^{-2}$  in the time-averaged  $s$  budget, with a standard deviation of  $14 \text{ W m}^{-2}$ . These errors are small compared to the vertical  $s$  advection term.

Utilizing these approximations and limiting vertical motion variability to two modes yields the following monthly column-integrated  $s$  budget:

$$LP \approx M_{s1} o_1(x, y, t) + M_{s2} o_2(x, y, t) - \Delta F_{\text{rad}}, \quad (4)$$

where the gross dry stratification for each mode  $i$ ,

$$M_{si} = \left\langle \Omega_i \frac{\partial s}{\partial p} \right\rangle, \quad i = 1, 2, \quad (5)$$

can be approximated as constant in space and time. The gross dry stratification of each mode, which is a measure of the adiabatic cooling per unit of modal amplitude, is calculated using the mean dry static energy profile over the tropical oceans in ERA-40 (the standard deviation

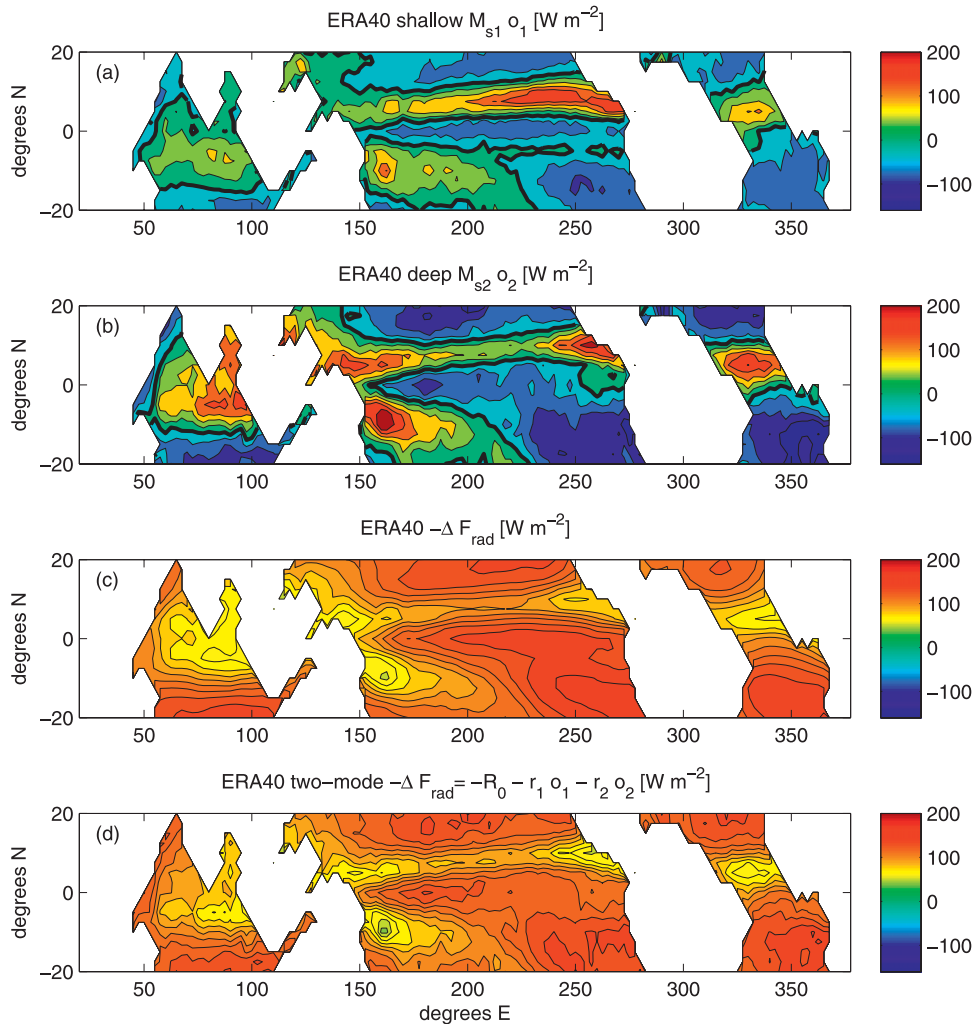


FIG. 3. 1998–2001 ERA-40 dry static energy budget by mode as in Eq. 4: (a) shallow-mode adiabatic cooling  $M_{s1}o_1$  and (b) deep-mode adiabatic cooling  $M_{s2}o_2$ , both with solid contour  $0 \text{ W m}^{-2}$ , contour interval  $30 \text{ W m}^{-2}$ ; (c) column-integrated radiative flux convergence  $\Delta F_{\text{rad}}$ , thick contour is  $-100 \text{ W m}^{-2}$ , contour interval  $10 \text{ W m}^{-2}$ ; and (d) reconstruction of  $\Delta F_{\text{rad}}$  from linear regression on shallow and deep modes [same contours as in (c)].

of the error introduced by approximating  $M_{si}$  as constant is only  $5 \text{ W m}^{-2}$ ). Since the amplitudes of the vertical structure functions,  $\Omega_{is}$ , are arbitrary and  $M_{si}$  depends on this choice, we present the modal amplitudes in terms of their equivalent adiabatic cooling  $M_{si}o_i(x, y, t)$  throughout our analysis.

Figures 3a,b show the geographic distribution of annual-mean adiabatic cooling due to the shallow and deep modes in ERA-40. Modal amplitudes  $o_i(x, y, t)$  were calculated by projecting ERA-40 monthly horizontal convergence profiles onto the modes. By construction, the geographic pattern of shallow mode cooling highly resembles the QuikSCAT surface wind convergence shown in Fig. 1. The deep mode is strongest over both hemispheres of the west Pacific warm pool

region and in the easternmost part of the Pacific ITCZ, which are regions with particularly warm SST (Fig. 1). This observation leads to the hypothesis developed in section 4 that the deep-mode distribution can be related to the underlying SST and the conditional instability of the overlying atmosphere.

The shallow- and deep-mode geographic patterns are visibly correlated. This has a sensible physical interpretation, which we will make use of in our prognostic model formulation. We expect shallow subsidence to inhibit the convective moistening necessary for deep-mode convection to erupt. This suggests that shallow-mode upward motion should be a necessary, but not sufficient condition for deep-mode convection and significant rainfall.

*b. Two-mode parameterization of ERA-40 column-radiative heating*

Atmospheric column-integrated radiative heating  $\Delta F_{\text{rad}}$ , shown in Fig. 3c, is a sizeable term in (4), though it varies much less than the adiabatic cooling because of the shallow and deep modes. This term can be divided into a clear-sky component  $R_0$  that is nearly constant within deep convective regions and a more variable warming term that is associated with longwave cloud-radiative forcing. A very simple way to treat the cloud-radiative forcing is to parameterize it as linearly dependent on rainfall (Peters and Bretherton 2005). However, higher clouds reduce clear-sky radiative cooling more than shallower clouds because of their colder cloud-top temperatures, so the spectrum of clouds associated with deep-mode ascent reduces radiative cooling more than the cloud spectrum associated with shallow-mode ascent. These differences are apparent when comparing cloud populations between the eastern and western Pacific as a function of rainfall (Kubar et al. 2007).

To incorporate differences in cloud-radiative forcing into the  $s$  budget, we parameterize the column-integrated radiative heating as a linear function of the two modes:

$$\Delta F_{\text{rad}} = R_0 + r_1 o_1 + r_2 o_2. \quad (6)$$

We estimate the constants  $r_1$  and  $r_2$  using a multiple linear regression between ERA-40 column-integrated radiative heating and the amplitudes of the two modes in ERA-40. To remain consistent with the ERA-40  $s$  budget, we use radiative cooling from ERA-40 instead of a satellite-derived product for this regression. With least squares fit coefficients  $r_1/M_{s1} = 0.06$ ,  $r_2/M_{s2} = 0.20$ , and  $R_0 = -113 \text{ W m}^{-2}$ , this fit explains 71% of the space-time variance of  $\Delta F_{\text{rad}}$ . Hence, radiative heating reconstructed from the two modes (shown in Fig. 3d) accurately captures the nature of the full ERA-40 radiative heating field.

We define effective stabilities that include cloud-radiative heating effects associated with the shallow and deep modes:

$$M_{sei} = \int_{p_0}^{p_i} \Omega_i \frac{\partial s}{\partial p} \frac{dp}{g} - r_i = M_{si} - r_i. \quad (7)$$

Using these effective stabilities, the relationship between precipitation and the amplitude of the two modes of variability can be expressed as

$$LP \approx M_{se1} o_1(x, y, t) + M_{se2} o_2(x, y, t) - R_0. \quad (8)$$

Cloud-radiative effects reduce the latent heating needed to balance the adiabatic cooling from a unit of vertical

motion ( $o_i$ ), because some of the extra adiabatic cooling is partly compensated by reduced radiative cooling. The reduction for mode  $i$  is  $r_i/M_{si}$ , which is 6% for the shallow mode (8% for NCEP) and 20% for the deep mode (14% in NCEP). Structure functions shown in Fig. 2d are normalized to correspond to the amount of vertical motion necessary to balance  $100 \text{ W m}^{-2}$  of latent heating. The solid, lesser-amplitude lines do not include cloud-radiative effects in this normalization, while the dashed, greater-amplitude lines have been normalized to account for the 20% (6%) feedback parameter.

The largest source of error in approximating (3) by (8) is the truncation of vertical motion profiles to two modes, which introduces a time-mean error with a standard deviation of  $25 \text{ W m}^{-2}$ . However, precipitation calculated using constant  $M_{sei}$  and the two-mode truncation explains almost all of the time-space variance in precipitation calculated as a  $s$ -budget residual from the right-hand side of Eq. (3) (i.e., 96%). As will be seen in the next section, reanalysis rainfall errors are a far greater source of uncertainty in the reanalysis heat budget.

#### 4. Predicting the deep mode in ERA-40

In BB09, we showed that the shallow-mode distribution (or equivalently climatological near-surface convergence) can be understood primarily as a forced response to SST gradients, though the 850-hPa fields, which may partially be a response to the global distribution of convection that also plays a role. In our two-mode view, the question “what determines the depth and intensity of deep convection induced by boundary layer convergence?” can thus be rephrased as “given the shallow-mode distribution, how is the deep-mode distribution determined?”

Previous research regarding deep convection over the tropical oceans has established that on synoptic time scales, the environmental humidity profile can be very important in determining the depth, intensity and lifetime of deep convection (DeMott and Rutledge 1998; Sherwood 1999; Bretherton et al. 2004; Sobel et al. 2004; Zuidema et al. 2006), while the role of more traditional factors like conditional instability as measured by CAPE is less clear. However, since on monthly time scales free-tropospheric moisture variability must largely be a consequence of the distribution deep convection, it should not be externally specified in a simple model of the distribution of rainfall and must be a part of the solution. One way to do this is to frame the model in terms of a quantity that is conserved in convecting regions, like moist static energy,  $h = C_p T + gz + Lq$ . However, as described in section 5 we abandoned such an approach because at least in ERA-40, it does not sufficiently

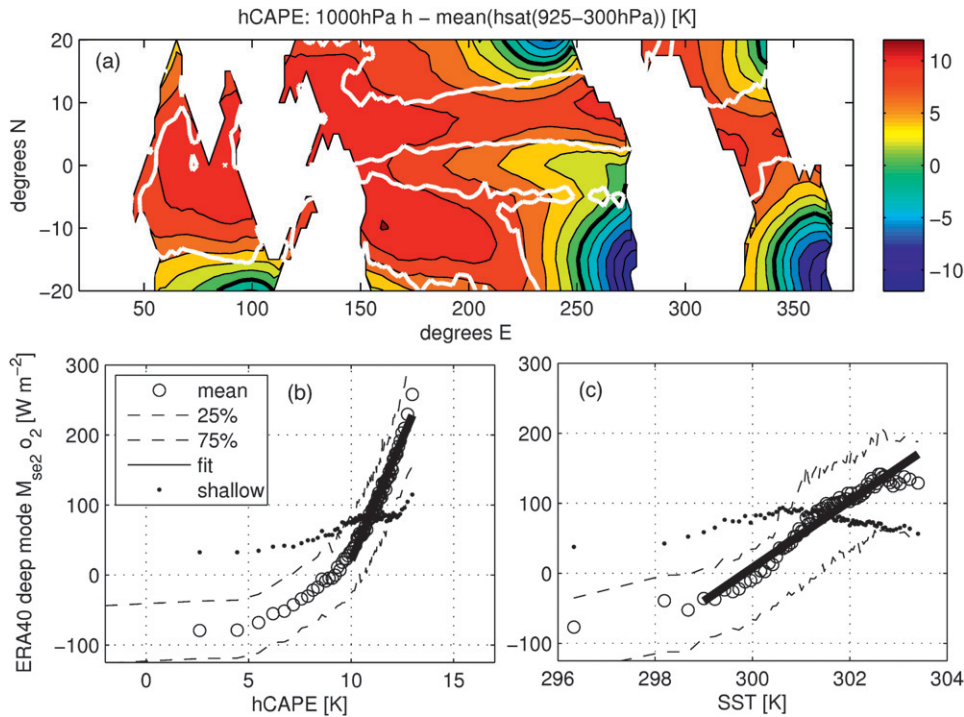


FIG. 4. (a) Time-mean ERA-40  $hCAPE/C_p$  as in (9), contour interval of 1 K, white contour denotes zero surface convergence. (b),(c) Monthly deep-mode adiabatic cooling,  $M_{s2O_2}$  binned in regions of shallow-mode ascent by (a)  $hCAPE$  or (b) SST. Each bin includes 500 gridpoint months. Open circles are bin-mean deep-mode cooling, lines are 25th and 75th percentiles within each bin. Dots are mean shallow-mode cooling for each bin. Solid black line is the linear fit in (10).

constrain the rainfall. Instead, we propose and test an alternative CAPE-based theory for the deep-mode amplitude.

A rationalization for the correlation between rainfall and SST embodied in the null hypothesis model is that SST varies much more than free-tropospheric temperature across the tropical oceans. Hence the warmest SSTs should correspond to the strongest and most persistent deep conditional instability, setting the stage for heavy mean rainfall. That is, rainfall is correlated with climatological CAPE. This idea is also supported by studies of the relationship between SST, CAPE, and rainfall (e.g., Bhat et al. 1996; Fu et al. 1994).

As we noted in the introduction, the null hypothesis model is broadly successful, but produces excessively broad rainfall belts, and does not explain geographic variability in the vertical structure of convection. In the previous section we noted a correlation between the ERA-40 deep and shallow modes. This can be physically interpreted as a requirement for monthly-mean boundary layer convergence, shallow-mode ascent, and lower-tropospheric moistening to support persistent deep-mode convection and significant monthly-mean rainfall. We will now show that if this requirement is met, the deep

mode is most active over the warmest SST regions and its amplitude is statistically correlated with a CAPE-like measure of column instability. Correspondingly, regions of monthly-mean shallow-mode descent and surface divergence tend to have insignificant rainfall. To close the two-mode  $s$  budget in such regions, deep-mode subsidence warming must balance the combination of radiative cooling and shallow-mode subsidence warming.

To test this idea, we calculate a climatological proxy for CAPE from ERA-40 (on monthly time scales), which we refer to as  $hCAPE$ :

$$hCAPE(x, y, t) = h(1000 \text{ hPa}, x, y, t) - \Delta p_F^{-1} \int_{p_{FT}}^{p_{FB}} h_{\text{sat}}(p, x, y, t) dp, \quad (9)$$

where  $h_{\text{sat}}$  is saturation MSE,  $p_{FB} = 925$  hPa,  $p_{FT} = 300$  hPa, and  $\Delta p_F = p_{FB} - p_{FT}$  are the nominal typical cumulus base, top, and layer thickness. Our model results (Fig. 5) are quite insensitive to an alternative choice of  $p_{FT} = 250$  hPa or  $p_{FT} = 150$  hPa. The sign of the measure  $hCAPE$  provides a rough lower bound on CAPE in deep convecting regions: we choose this measure because surface data is not available from the reanalysis and this

is a convenient metric (for the case  $p_{FB}$  is the lifting condensation level and  $p_{FT}$  is the level of neutral buoyancy, assuming pseudoadiabatic ascent from 1000 hPa, neglecting virtual temperature effects and taking  $dP \propto dP/T$ , hCAPE is exactly proportional to CAPE as defined in Emanuel (1994)).

As seen in Fig. 4, positive hCAPE, indicating climatological deep conditional instability to pseudoadiabatic ascent of 1000-hPa air, is present throughout the oceanic ITCZs, but also over many lower-SST regions in which there is little mean rainfall. Thus, the sign of hCAPE is not by itself adequate to explain the location of the rainfall belts.

SST and hCAPE are strongly correlated, since tropical free-tropospheric temperature variations are much smaller than those in the boundary layer. The best-fit linear relationship between hCAPE and SST, which explains 70% of the space–time variance in hCAPE, is

$$\frac{\text{hCAPE}}{c_p} = 2.36(\text{SST} - 296 \text{ K}).$$

We sorted ERA-40 monthly averaged gridpoint shallow- and deep-mode amplitudes in regions of shallow-mode ascent by hCAPE and averaged them into bins each containing 500-gridpoint-month boxes. Figure 4b shows bin-mean deep- and shallow-mode adiabatic cooling plus associated cloud-radiative effects, as well as deep-mode quartiles. The amplitude of the deep mode is strongly related to hCAPE (binning explains 37% of the variance). The relationship is nonlinear with a comparatively low slope at low values of hCAPE  $< 10$  K and a steeper slope at high values of hCAPE  $> 10$  K. In con-

trast, variations in the amplitude of the shallow mode are only weakly related to hCAPE (binning explains only 5% of the variance).

Figure 4b also shows a least squares linear fit:

$$\begin{aligned} M_{se2}o_2(x, y) &= aC_h(x, y) + b, \quad C_h = \text{hCAPE} > 10 \text{ K}, \\ a &= 56.9 \text{ W m}^{-2} \text{ K}^{-1}, \quad b = -526.7 \text{ W m}^{-2}. \end{aligned} \quad (10)$$

This fit explains 26% of the space–time variance of the deep-mode amplitude in regions with hCAPE  $> 10$  K.

From (8), one can see that if  $o_2(x, y, t)M_{se2} < R_0 - M_{se1}o_1(x, y, t)$ , precipitation goes below zero, an unphysical solution. Physically, in the zero precipitation case, subsidence warming balances radiative cooling. The low hCAPE cases where the linear fit is weak in Fig. 4b correspond to this case.

Figure 4c shows the same analysis performed with SST as the independent variable instead of hCAPE. The correlation with rainfall is weaker ( $r^2 = 20\%$ ), and the nonlinearity less apparent, but similar in nature, demonstrating that in this respect SST is a reasonable climatological proxy for hCAPE over the tropical oceans.

We are now ready to predict the amplitude of the deep mode given the shallow-mode amplitude in ERA-40. Within shallow-ascent regions, the deep-mode amplitude is determined by hCAPE using (10), unless the linear fit predicts negative rainfall, in which case rainfall is assumed to be zero and the energy-balance constraint is invoked to determine the deep-mode amplitude. In shallow subsidence regions, the assumption of zero rainfall determines the deep-mode amplitude:

$$M_{se2}o_2(x, y, t) = \begin{cases} aC_h(x, y, t) + b & \text{if } C_h(x, y, t) > \frac{R_0 - o_1M_{se1} - bM_{se2}}{aM_{se2}} \\ & \text{and } o_1(x, y, t) > 0 \\ R_0 - M_{se1}o_1(x, y, t) & \text{otherwise.} \end{cases} \quad (11)$$

We predict the deep mode from (11) for each grid point over each of the 48 months used. Figure 5 shows the resulting time-mean deep-mode adiabatic cooling. The pattern correlation between this prediction and the ERA-40 deep mode (Fig. 3) is very high ( $r = 0.82$ ); on monthly time scales these patterns also are strongly correlated in space–time ( $r = 0.65$ ).

Combining this deep-mode prediction and knowledge of the shallow mode, we can predict the rainfall distribution. The time-mean rainfall derived as a residual from the right-hand side of (3), shown in Fig. 5c, compares very well (time mean  $r = 0.94$ , monthly space–time

$r = 0.83$ ) to the two-mode rainfall prediction shown in Fig. 5b, derived from (11) and (8) based only on ERA-40-derived hCAPE and shallow-mode amplitude (though precipitation is somewhat underestimated in the Atlantic, eastern Pacific, and Indian Ocean because of the predicted deep mode being weaker than in ERA-40 in these regions.)

Two obstacles to applying these ERA-40 derived formulas are that the reanalysis  $s$  budget does not close and that ERA-40 rainfall tends to be considerably larger than satellite retrievals. Figure 5d shows reanalyzed precipitation from ERA-40 in energy flux units,

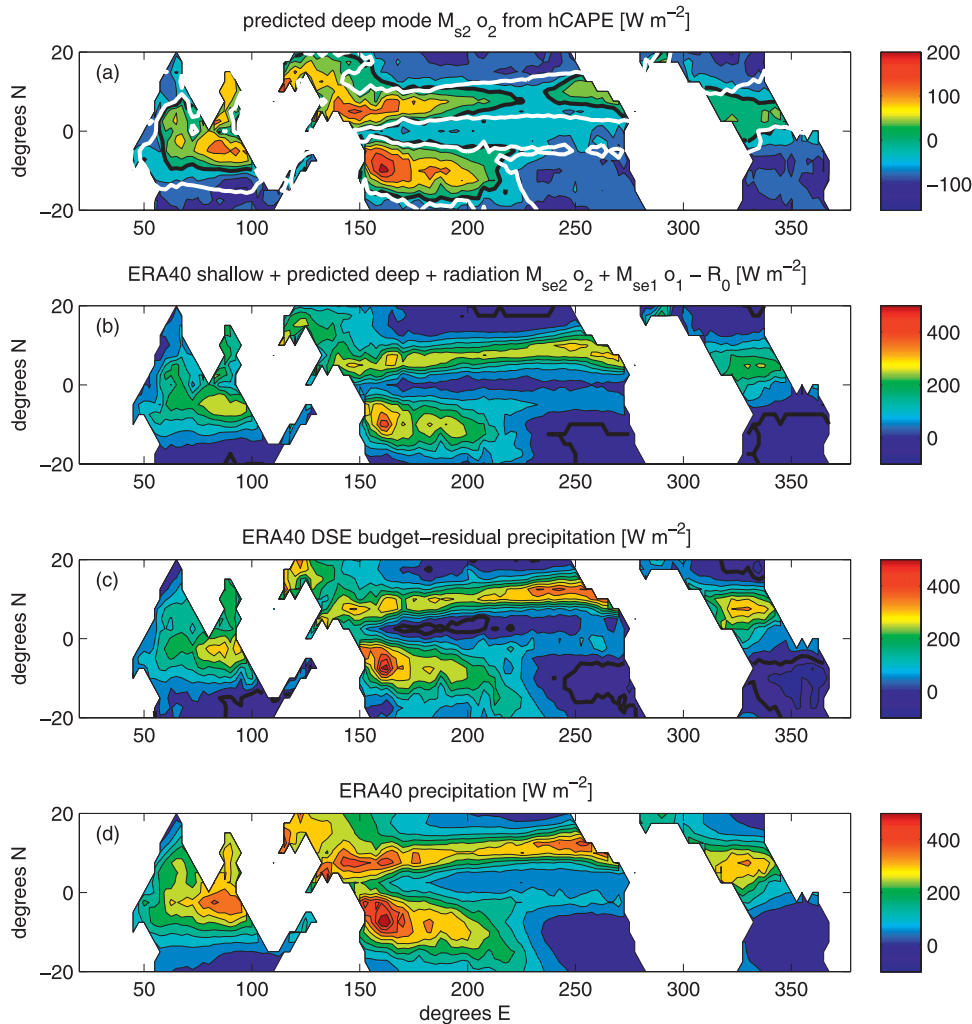


FIG. 5. Time mean (a) deep-mode amplitude predicted from (11), same contour interval,  $30 W m^{-2}$ , and color scale as Fig. 3a. (b) Total precipitation as in (8) implied by this prediction, (c) precipitation required to balance full ERA-40 dry static energy budget in (3), and (d) ERA-40 precipitation. (a)–(d) All are in energy flux units and (b)–(d) have contour intervals  $50 W m^{-2}$ . The zero contour is solid black. The zero shallow-mode amplitude is shown with a white contour in (a):  $29 W m^{-2} \approx 1 mm day^{-1}$ .

which is appreciably different from the  $s$  budget-residual precipitation shown in Fig. 5c. Both of these estimates of the precipitation in ERA-40 show that ERA-40 overestimates precipitation by about 50% compared to observations (Fig. 1a). The figures also illustrate that the heat budget in the reanalysis is unbalanced, with a geographically varying residual. In some deep convective regions, the reanalysis has a strong cooling tendency term likely associated with assimilation of observations nudging the reanalysis toward cooler tropospheric temperatures. These biases also demonstrate the difficulties reanalyses have in simulating a realistic tropical state.

The skill with which a simple function of hCAPE and shallow-mode amplitude can reproduce the reanalysis

vertical motion fields and  $s$  budget suggests that our two-mode framework is useful. However, the lack of closure and excessive implied rainfall in the reanalysis-simulated  $s$  budget suggests that retuning of constants may be required to match observations.

### 5. Column-integrated moist static energy budget constraints?

Column-integrated moist static energy budgets have been an attractive theoretical proposal for understanding the geographic distribution of deep convection and its interaction with large-scale tropical circulations (Neelin and Held 1987; Neelin and Zeng 2000; Sobel and Neelin 2006). Unlike the statistical relationships discussed above,

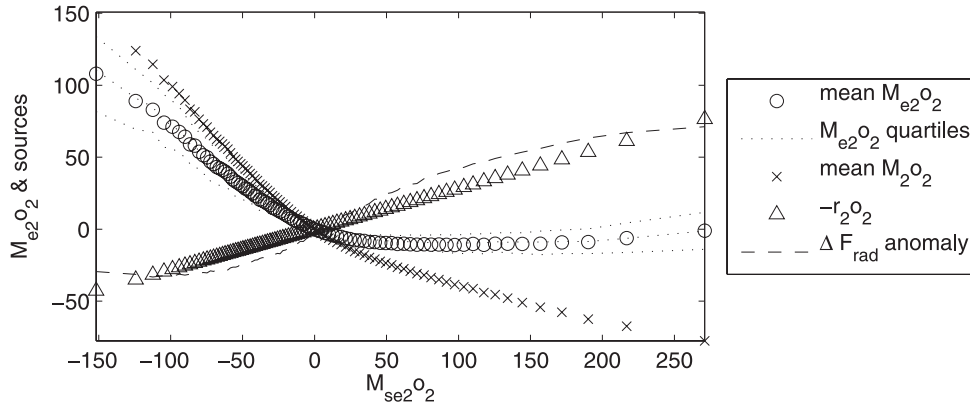


FIG. 6. Deep-mode contribution to column-integrated MSE budget,  $M_{e2}o_2$ , binned by deep-mode amplitude  $M_{s2}o_2$  (500-gridpoint-month bins). Bin mean and quartiles are shown by circles and dotted lines respectively. The contribution from  $M_2o_2$  is shown by  $\times$ 's and the largely canceling cloud-radiative contribution  $-r_2o_2$  is shown with triangles.

such an approach could include the effects of horizontal moisture advection, which may substantially influence the geographic distribution and/or amount of deep convection (e.g., Sobel and Bretherton 2000; Back and Bretherton 2006). We originally intended to use such a framework to predict the deep-mode amplitude given a specification of the shallow mode. However, using the above two-mode truncation, we found that the MSE budget does not usefully constrain the deep-mode amplitude. The problem with using the MSE budget as a constraint, as we elaborate on below, is that at least in ERA-40, the deep-mode effective gross moist stability (including cloud-radiative feedbacks) is nearly zero, so the MSE budget is extremely insensitive to the deep-mode amplitude.

The full column-integrated moist static energy ( $h = s + Lq$ ) budget (e.g., Back and Bretherton 2006) is (before averaging in time)

$$\left\langle \frac{\partial h}{\partial t} \right\rangle = \left\langle -u \frac{\partial h}{\partial x} - v \frac{\partial h}{\partial y} \right\rangle + \left\langle -\omega \frac{\partial h}{\partial p} \right\rangle + F_{\text{turb}}^h(0) + \Delta F_{\text{rad}} + R_h.$$

In order, the terms in the column-integrated MSE budget are storage, horizontal advection, vertical advection, surface fluxes, radiation, and a residual, and the brackets indicate mass-weighted vertical integrals. Truncated to the two modes derived from ERA-40 in section 3, neglecting the residual and assuming steady state, the monthly-mean column-integrated MSE budget can thus be written as a prognostic equation for the deep-mode contribution to the MSE budget, given “forcing” by the shallow mode, horizontal advection, surface fluxes, and transients (eddies):

$$M_{e2}o_2 = -M_{e1}o_1 + \left\langle -u \frac{\partial h}{\partial x} - v \frac{\partial h}{\partial y} \right\rangle - R_0 + F_{\text{turb}}^h(0) + \text{transients}, \quad (12)$$

where the gross moist stabilities  $M_i$  and effective gross moist stabilities  $M_{ei}$  (including cloud-radiative feedbacks) for the two modes are defined as in (7):

$$M_i = \left\langle \Omega_i \frac{\partial h}{\partial p} \right\rangle, \quad (13)$$

$$M_{ei} = M_i - r_i. \quad (14)$$

With known terms on the right-hand side of (12) and known modal effective gross moist stabilities, this equation could be used to determine how much deep-mode convection occurs, which would then determine rainfall via (8). Unlike for the dry stability  $M_{s2}$ , the assumption that  $M_2$  is horizontally uniform is inappropriate since this quantity depends on free-tropospheric moisture (which is highly variable) as well as  $s$ . For present purposes,  $M_2$  was computed separately from (13) at each gridpoint month using the thermodynamic profiles in ERA-40, and  $M_{e2}$  was deduced from (14).

The problem with using (12) as a prognostic equation for deep-mode amplitude can be seen by calculating the left-hand side of (12) from ERA-40 at each gridpoint-month as the product of the above estimate of  $M_{e2}$  with the ERA-40 deep-mode amplitude  $o_2$ . Figure 6 shows values of  $M_{e2}(x, y, t)o_2(x, y, t)$  sorted and binned into 500-gridpoint-month bins by deep-mode amplitude, expressed as an equivalent adiabatic cooling  $M_{s2}o_2(x, y, t)$ . When  $o_2$  is positive, as must be the case when the deep-mode contributes to precipitation, the average  $M_{e2}o_2$  is almost identically zero.

The figure also shows that the zero effective gross moist stability represents a near-perfect cancellation between the two contributions  $M_2o_2$  and  $-r_2o_2$ . Also shown is an alternative estimate of  $o_2r_2$  calculated as the residual:  $\Delta F_{\text{rad}}$  anomalies. In both cases, the extent of the cancellation seems remarkable and merits further exploration. It implies that, at least using this set of basis modes and ERA-40 thermodynamic profiles, the deep mode is on average a negligibly small contributor to the column-integrated MSE budget, so the deep-mode amplitude cannot be meaningfully constrained in this way. In NCEP, the deep-mode contributes more to the column-integrated MSE budget (not shown) because it is more “top heavy” (see Fig. 2).

The above result may at first seem to be in contradiction with the success of simple tropical models based on the column-integrated moist static energy budget at simulating the first-order distribution of rainfall (e.g., Neelin and Zeng 2000). However, it is known that this family of models is quite sensitive to the assumed gross moist stability (e.g., Yu et al. 1998), a parameter that is not well constrained observationally (Back and Bretherton 2006), and that must be specified in these models. Including strong cloud-radiative effects in this type of model when SST is specified can also cause the solution to blow up (Sobel et al. 2004). The two-mode system we examined corresponds to this type of case;  $M_2$  is small in convecting regions, so as rainfall increases, the increased export of moist static energy by the vertical circulation,  $M_2o_2$  is nearly balanced by reduced outgoing longwave radiation due to clouds, and hence increasing the deep-mode amplitude does not increase the deep-mode contribution to the column-integrated  $h$  budget.

## 6. Rainfall prediction using QuikSCAT to specify the shallow mode

Given the substantial precipitation biases seen in ERA-40, other reanalyses and AGCMs, it is desirable to test the two-mode model using reanalysis-independent data. For this purpose, we use monthly QuikSCAT surface convergence, SST observations, and GPCP rainfall observations from 2000–01 to examine the extent to which a two-mode model with QuikSCAT surface convergence determining the shallow-mode amplitude and SST determining the deep-mode amplitude can predict tropical rainfall patterns. This is obviously not a closed theory because we are specifying surface convergence, but it tests whether surface convergence does indeed add to the skill of an SST-based rainfall prediction, as our analysis of the ERA-40  $s$  budget suggested.

Using QuikSCAT surface convergence  $o_q(x, y, t)$  as a proxy for the shallow-mode amplitude, the monthly rainfall predicted by (11) and (8) has the following form:

$$LP = \begin{cases} H[o_q(x, y, t)]\{a_s o_q(x, y, t) + b_s [T_s(x, y, t) - c_s]\} \\ \quad \text{if } T_s > -a_s o_q(x, y, t)/b_s + c_s \\ 0 \quad \text{otherwise.} \end{cases} \quad (15)$$

The constants  $a_s$ ,  $b_s$ , and  $c_s$  can be deduced from the parameters  $a$ ,  $b$ ,  $M_{se1}$ , the relationship between hCAPE and SST, and a regression between  $o_q$  and  $M_{se1}o_1$ . Using these estimated parameters ( $a_s = 2.1 \times 10^7 \text{ W m}^{-2} \text{ s}$ ,  $b_s = 102.3 \text{ W m}^{-2} \text{ K}^{-1}$ , and  $c_s = 293 \text{ K}$ ) produces a similar 2-yr mean to that shown in Fig. 5b, which matches the ERA-40  $s$ -budget-inferred rainfall but is much higher than the GPCP-observed rainfall for the same period in most locations. Hence, we use an interactive nonlinear optimization procedure (as in the null hypothesis model) to find values  $a_s = 1.5 \times 10^7 \text{ W m}^{-2} \text{ s}$ ,  $b_s = 31.1 \text{ W m}^{-2} \text{ K}^{-1}$ , and  $c_s = 297.17 \text{ K}$  that minimize the root-mean-square error in the 2-yr mean precipitation as compared to GPCP.

Two-year mean precipitation predicted from monthly QuikSCAT surface convergence and SST observations using these parameters is shown in Fig. 7a. Figure 7b shows GPCP precipitation for the same time period. The second column of Table 1 summarizes the skill of this optimized model as compared to observations under the heading “qSCAT.” The correlation with GPCP is 0.92, which compares favorably with the correlation of 0.77 produced by the null hypothesis model (SST regression only), and with the climatologies of current-generation U.S. AGCMs forced by observed SSTs. For monthly anomalies from the 2-yr mean, the correlation coefficient is 0.77, compared to 0.61 for the null hypothesis model.

As in the observations, time-mean precipitation maxima occur in the Northern Hemisphere eastern Pacific and the western Pacific has a climatological double ITCZ. In the Atlantic and Indian Ocean basins, the precipitation maxima are also correctly placed, though too weak. The largest discrepancies are in the southwestern Pacific, where the predicted precipitation region extends farther to the east than in observations. Horizontal dry advection, a factor that could potentially strongly influence precipitation patterns and is not a part of this model, is particularly strong in the southwestern Pacific ITCZ region in ERA-40 (Back and Bretherton 2006), and may be responsible for this particular model bias. Predicted rainfall is also somewhat too weak over the Indian Ocean and northwest Pacific, for reasons that we do not fully understand.

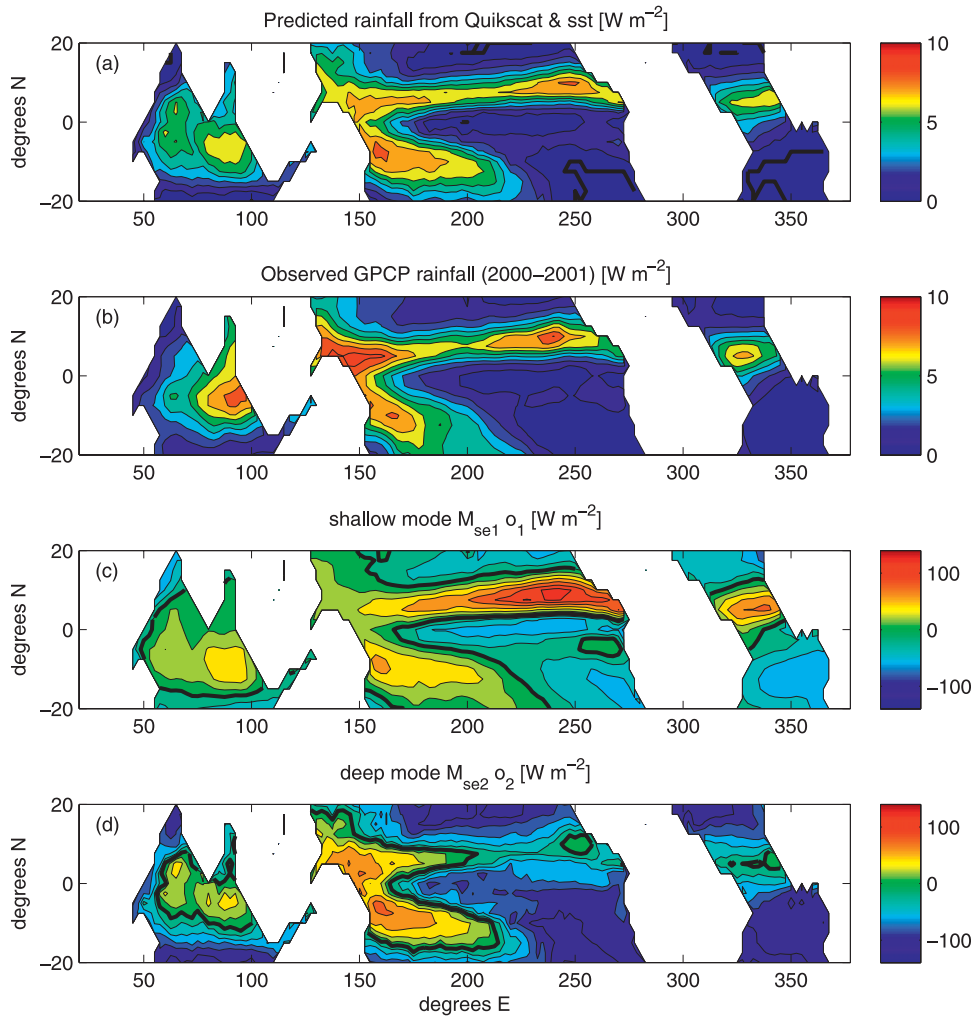


FIG. 7. (a) 2000–01 two-mode model mean precipitation predicted from (15) using monthly  $2.5^\circ$  Quikscat convergence and SST, and (b) GPCP rainfall, both with contour intervals of  $1 \text{ mm day}^{-1}$ . (c) Shallow-mode ( $o_1 M_{s1}$ ) and (d) deep-mode ( $o_2 M_{s2}$ ) components of (a). The contour interval is  $20 \text{ W m}^{-2}$ .

The predicted rainfall pattern is also associated with shallow- and deep-mode amplitudes (Figs. 7c,d). As previously, shallow- and deep-mode amplitudes are normalized to show adiabatic cooling rates ( $M_{si}o_i$ ).

Predicted atmospheric column-radiative cooling associated with the predicted shallow- and deep-mode amplitudes (Fig. 8a) is also broadly similar to the ISCCP satellite-retrieved radiative flux convergence (Fig. 8b). The spatial correlation coefficient of time-mean-observed and predicted radiative cooling is 0.79. Our two-mode parameterization of cloud-radiative effects has been designed to capture variations in flux divergence within regions of deep convection, where cloud-radiative effects should be most correlated with the vertical motion profiles. Hence, in regions of mean convergence, shown by the thick line in Fig. 8, the agreement between the ISCCP retrievals and the two-

mode prediction is substantially better than in regions of divergence where enhanced radiative cooling due to shallow clouds can be quite important. A simple way to improve the parameterization of radiative cooling in this type of model would be to add additional atmospheric cooling proportional to  $c(T_s - T_c)H(T_c - T_s)$ , where  $T_c$  is a critical SST below which shallow clouds are assumed to form, and  $T_c$  and  $c$  are tuning parameters (Peters and Bretherton 2005).

To examine the direct precipitation contribution of each mode to the total precipitation, predicted precipitation from this model can alternatively be decomposed by adding the radiative heating and adiabatic contributions from each mode, as in (15). A component  $H(LP)a_s o_q$  is directly due to the shallow mode, the term  $H(LP)M_{se2} o_2$  is directly due to the deep mode, and the remaining precipitation is required to

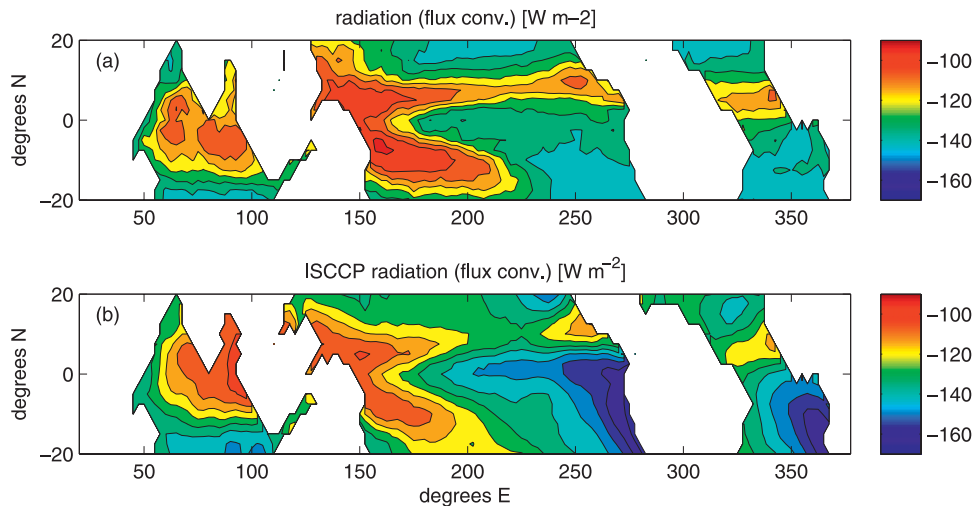


FIG. 8. (a) Time-mean atmospheric radiative flux convergence predicted by two-mode model using observed convergence and SST, and (b) comparable ISCCP satellite retrievals for 2000–01.

balance the tropical-average radiative cooling rate  $R_0$ . The  $b_s(T_s - c_s)$  term in (15) combines the latter two quantities. Figure 9 shows the precipitation decomposed in this manner, where the  $M_{se2}$  and  $R_0$  values derived from ERA-40 are used to separate between the radiative-convective equilibrium contribution ( $R_0$ ) and the deep-mode contribution. The decomposition shows that the shallow and deep modes contribute roughly equally to the precipitation distribution in this model. However, including the shallow mode as we have done in predicting precipitation substantially alters the distribution of precipitation from the null hypothesis model due to the condition that shallow-mode ascent is required for precipitation to occur. Much of the rainfall that occurs balances mean radiative cooling and is not directly associated with large-scale upward vertical motion profiles.

## 7. Rainfall based on MLM-predicted convergence

In BB09, we demonstrated the skill of a simple mixed-layer model at modeling surface convergence patterns from SST, supplemented by 850-hPa temperature, horizontal winds, and geopotential height gradients. Combining such a prediction of the shallow mode with predictions of the deep mode allows precipitation predictions from the boundary layer model inputs alone. It can also potentially be used to quantify how free-tropospheric tropical temperature gradients and winds (which are a response to global-scale low-latitude latent heating patterns) feed back on precipitation patterns.

Figures 10a,b show precipitation climatologies computed by using the MLM and MLM-SST to predict

surface convergence and using (15) to derive corresponding rainfall patterns. As detailed by BB09, the inputs to the MLM are surface pressure and 850-hPa winds, while the MLM-SST uses SST together with 850-hPa temperature, geopotential height, and horizontal winds as input. The right two columns of Table 1 summarize the skill of these models in predicting time-mean precipitation. As one would expect, correlation coefficients based on the MLM are slightly better than with the MLM-SST, but not as good as when surface convergence is observationally specified. In fact the MLM-SST has skill scores only slightly improved over the SST-only null hypothesis model. However, the error structure is quite different. The MLM-predicted rainfall bands are narrower than SST maxima, as in observations. The MLM solutions seem to go too far in this direction. Furthermore, a strong “double ITCZ” bias is present in the MLM-predicted rainfall.

Unlike the null hypothesis model, the two-mode model predicts vertical structure of latent heating and cloud-radiative effects in addition to rainfall. As a first guess, we use the modes of variability derived from ERA-40 to approximate the vertical motion profiles predicted by the qSCAT, MLM, and MLM-SST precipitation solutions. We then examine the regions in which both reanalyses and AGCM’s robustly reproduce bottom-heavy and top-heavy vertical motion profiles (Back and Bretherton 2006). Figure 11 shows predicted vertical motion profiles in selected regions in the central-eastern Pacific ITCZ and over the western Pacific warm pool. These regions are nearly identical to those used by Back and Bretherton (2006) to illustrate geographic variability in vertical motion profiles (one eastern Pacific

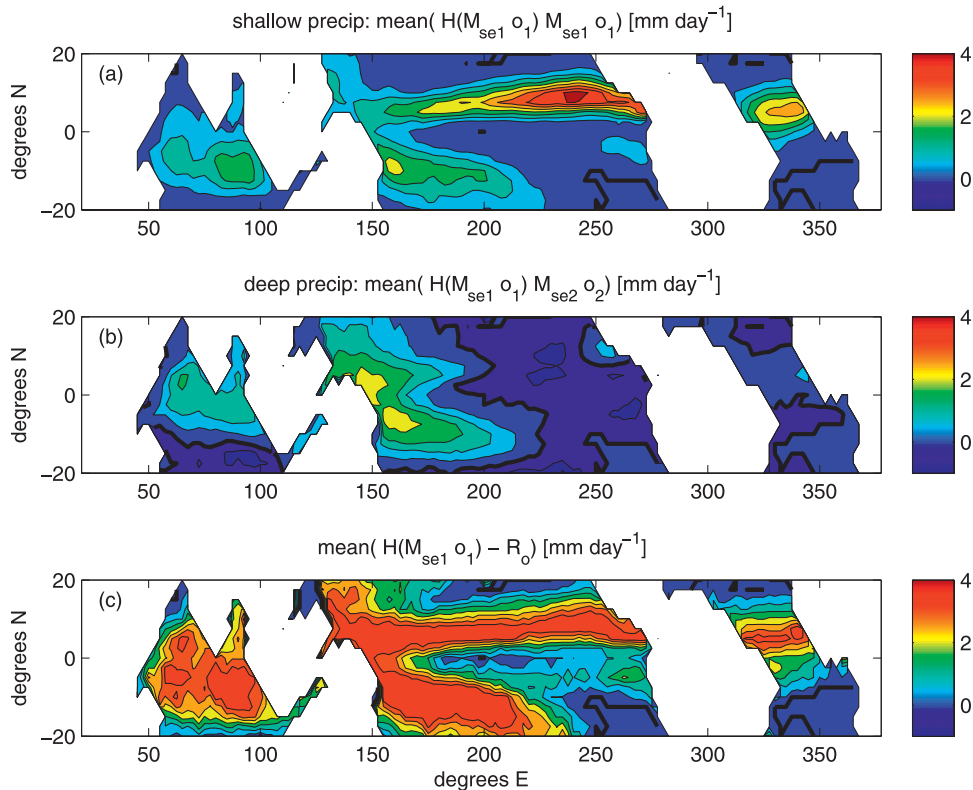


FIG. 9. (a) Precipitation contribution from the shallow mode (average of  $M_{se1}o_1$  in rainy regions, with zeros averaged in nonrainy regions), (b) deep-mode contribution (average of predicted  $M_{se2}o_2$  in regions with surface convergence, zeros averaged in nonrainy regions), and (c) rainfall required to maintain radiative-convective equilibrium (average of  $-R_0$  in rainy regions and zero in nonrainy regions). The contour interval  $0.5 \text{ mm day}^{-1}$ .

grid point is too close to land to accurately compute the MLM solution). The ERA-40 vertical motion profiles are normalized to balance the diabatic heating implied by GPCP rain rates.

The two-mode solutions capture and explain the contrast in the vertical motion profile differences that were observed by that study. In the central-eastern Pacific ITCZ, strong SST gradients drive surface convergence and low-level vertical motion. SST, though only 1–2 K cooler than in the western Pacific, is not warm enough to support a substantial amount of deep-mode convection, so the strong shallow mode in combination with a weak deep mode causes bottom-heavy vertical motion. Over the western Pacific warm pool, SST gradients and surface convergence are substantially weaker and deep-mode convection is much stronger because of the warmer SST. This results in a comparatively top-heavy vertical motion profile.

#### Seasonal cycle

The statistical relationships used in constructing the two-mode models should apply to seasonal precipitation

anomalies as well as the annual mean precipitation. Precipitation is an inherently noisy quantity, and on seasonal time scales it is natural to expect some stochastic variability that is not predictable from the SST and surface convergence fields alone. However, it is meaningful to ask how well our model can predict the seasonal cycle of precipitation averaged over several years.

Figure 12 shows a typical example of predicted seasonal precipitation anomalies compared to the observations. The anomalies shown are for September–November 1998–2001 (2000–01 for QuikSCAT), where anomalies were computed with respect to the predicted or observed climatology. All our two-mode models reproduce the general nature of the precipitation anomalies seen in the observations over the Atlantic and Pacific basins better than the null hypothesis model. The bottom row of Table 1 summarizes the combined spatial and seasonal correlation coefficient of the modeled seasonal precipitation anomalies compared to GPCP. As in the annual mean case, the correlations of the two-mode model predictions with GPCP are an improvement over

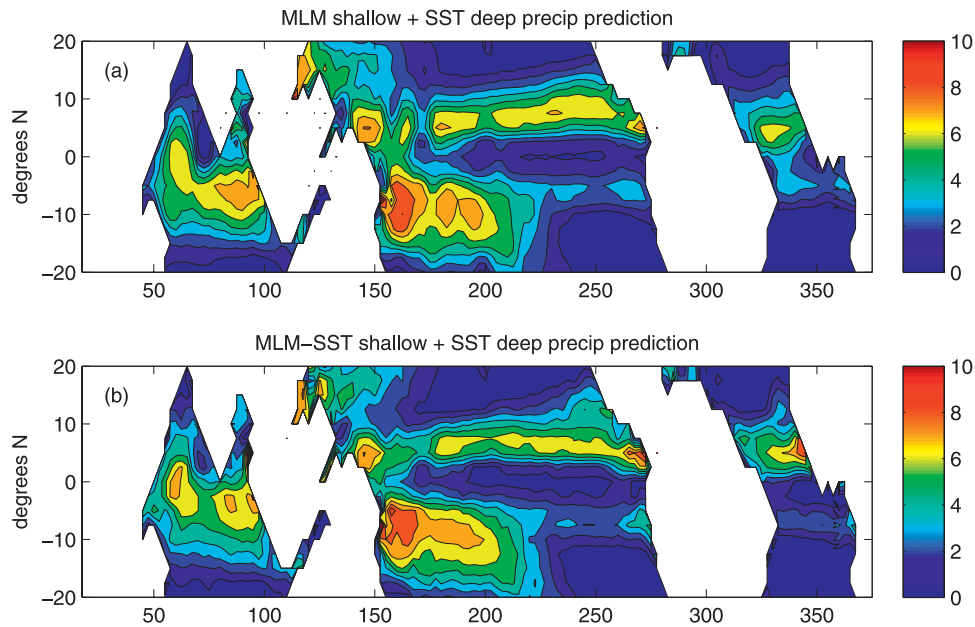


FIG. 10. 1998–2001 mean two-mode model precipitation using (15) based on surface convergence predicted from MLM (a) and (b) MLM-SST.

the null hypothesis (albeit slight for MLM-SST), and the predicted rainfall anomalies are realistically larger and more focused.

## 8. Discussion and conclusions

We have shown that a simple two-vertical mode model based on SST and surface convergence can explain a substantial fraction of the observed variability in rainfall, vertical motion, and latent heating profiles over the warm tropical oceans. In the model, surface convergence is associated with a shallow mode of convection that is lin-

early proportional to surface convergence in both regions of convergence and divergence. The amplitude of a deep mode of convection increases linearly with SST in regions with surface convergence. In regions with surface divergence, the deep-mode subsidence is determined by the constraint that when precipitation is zero, column-integrated subsidence warming must balance radiative cooling. Addition of surface convergence as a predictor substantially increases the skill of the rainfall distribution that would be predicted from a regression on SST alone, and is crucial to prediction of top or bottom heaviness of the vertical motion and diabatic heating profiles.

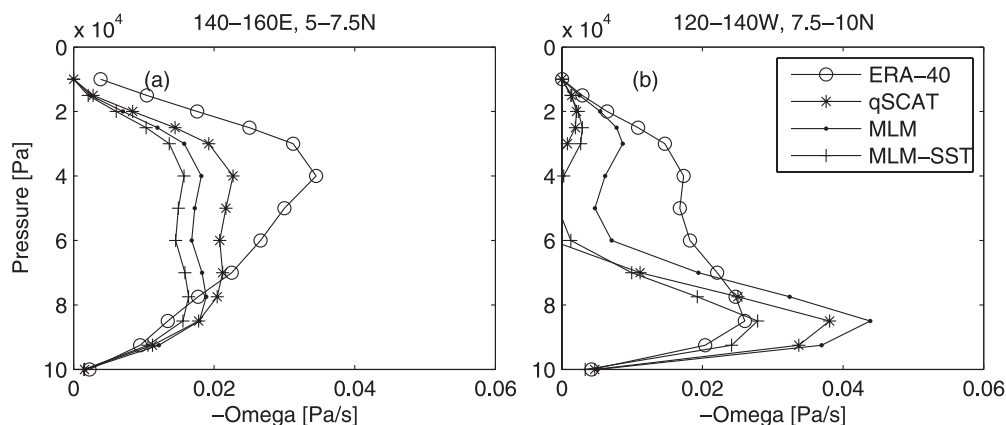


FIG. 11. Predicted vertical motion profiles using surface convergence from QuikSCAT, MLM, and MLM-SST compared to ERA-40 vertical motion profiles normalized to GPCP rain rates in (a) western Pacific warm pool region and (b) central-eastern Pacific ITCZ.

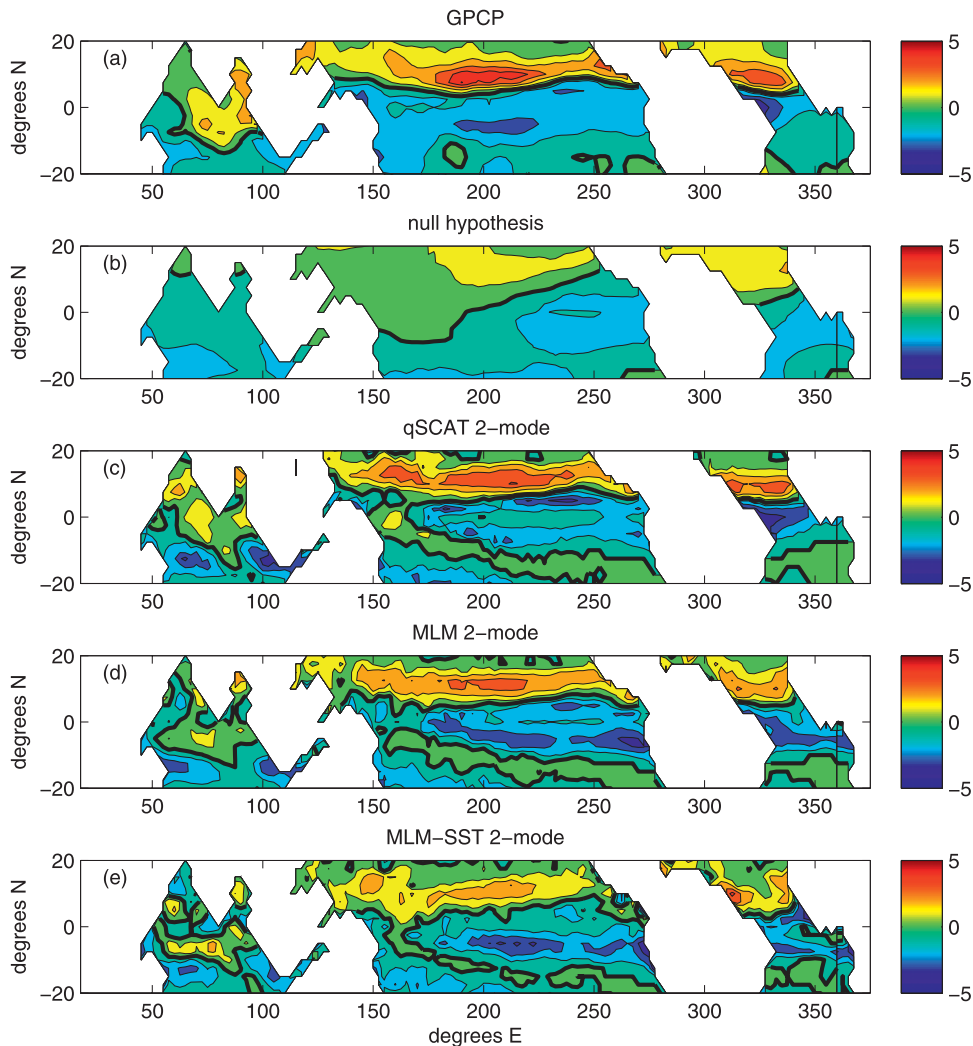


FIG. 12. September–November seasonal precipitation anomalies from predicted or observed annual mean, for 1998–2001 unless otherwise stated: (a) GPCP observations, (b) null hypothesis, (c) two-mode model using QuikSCAT surface convergence for 2000–01, (d) two-mode model using MLM-predicted convergence based on surface pressure, and (e) two-mode model using MLM–SST.

BB09 showed that boundary layer convergence depends mainly on gradients of SST. However, their analysis also suggested that the global distribution of deep convective heating feeds back nonlocally on boundary layer convergence by influencing free-tropospheric temperature and winds. This feedback could perhaps also be modeled based on the broadscale SST and continent/ocean distribution (using a Gill-type model), combined with the present two-mode model.

Our model suggests that the observed geographic variability in tropical vertical motion (and hence diabatic heating and cloud vertical distribution) profiles can be understood mainly as the consequence of the geographic variability in SST gradients and the magnitude of the underlying SST. In particular, the bottom-heavy vertical

motion profiles in the central-eastern Pacific ITCZ are due to the strong surrounding SST gradients and the lower SST than in more top-heavy regions like the western Pacific warm pool.

We have specified SST in this study, but the two-mode model can also provide insight into the observed variability in SST within deep convective regions. In particular, SST is somewhat lower in the central-eastern Pacific ITCZ than in the west Pacific warm pool, even though the two regions have comparable oceanic heat export, column-integrated horizontal moisture advection, and surface latent heat fluxes (in ERA-40). This can be explained with a two-mode variation of a cloud-shading feedback argument invoked by Ramanathan and Collins (1991), Peters and Bretherton (2005), and

others. The strong SST gradients between the equatorial cold tongue and the east Pacific ITCZ help drive shallow-mode ascent in that region. This creates a bottom-heavy contribution to the cloud distribution, which strongly shades the sea surface. Thus, the surface energy budget will balance with less deep-mode shading. Since deep-mode amplitude (and hence shading) increases with SST, we conclude that the equilibrium SST will be somewhat lower in the ITCZ than in the warm pool.

Our model includes empirical constants associated with an implied sensitivity of time-mean deep-mode convection to the underlying SST. This sensitivity could be compared to that of a given convective parameterization, or a cloud-resolving model using the weak temperature gradient approximation and the observed tropical stratification, as was done for example by Sobel and Bretherton (2000) and Sobel et al. (2007). Interestingly, the sensitivity of rainfall to SST is substantially lower in our empirical model than that implied by these previous studies, suggesting that this is a worthy topic for future study.

*Acknowledgments.* This work was supported by Grant DE-FG02-05ER63959 from DOE's ARM program and Grant NA06OAR4310055 from the NOAA/CPPA program. Thanks to Matt Wyant for help with processing data, and Dennis Hartmann and Robert Wood for comments on an earlier version of this work, which was included in the first authors doctoral dissertation. We thank the reviewers for providing comments that improved this work.

#### REFERENCES

- Adler, R. F., and Coauthors, 2003: The version-2 Global Precipitation Climatology Project (GPCP) monthly precipitation analysis (1979–present). *J. Hydrometeorol.*, **4**, 1147–1167.
- Back, L. E., and C. S. Bretherton, 2006: Geographic variability in the export of moist static energy and vertical motion profiles in the tropical Pacific. *Geophys. Res. Lett.*, **33**, L17810, doi:10.1029/2006GL026672.
- , and —, 2009: On the relationship between SST gradients, boundary layer winds, and convergence over the tropical oceans. *J. Climate*, **22**, 4182–4196.
- Battisti, D. S., E. S. Sarachik, and A. C. Hirst, 1999: A consistent model for the large-scale steady surface atmospheric circulation in the Tropics. *J. Climate*, **12**, 2956–2964.
- Bhat, G. S., J. Srinivasan, and S. Gadgil, 1996: Tropical deep convection, convective available potential energy and sea surface temperature. *J. Meteor. Soc. Japan*, **74**, 155–166.
- Bjerknes, J., 1969: Atmospheric teleconnections from the equatorial Pacific. *Mon. Wea. Rev.*, **97**, 163–172.
- Bony, S., K. Lau, and Y. Sud, 1997: Sea surface temperature and large-scale circulation influences on tropical greenhouse effect and cloud radiative forcing. *J. Climate*, **10**, 2055–2077.
- Bretherton, C. S., and D. L. Hartmann, 2008: Large-scale controls on cloudiness. *Clouds in the Perturbed Climate System: Their Relationship to Energy Balance, Atmospheric Dynamics, and Precipitation*, J. Heintzenberg and R. J. Charlson, Eds., MIT Press, 217–234.
- , M. E. Peters, and L. E. Back, 2004: Relationships between water vapor path and precipitation over the tropical oceans. *J. Climate*, **17**, 1517–1528.
- Chan, S., and S. Nigam, 2009: Residual diagnosis of diabatic heating from ERA-40 and NCEP reanalyses: Intercomparisons with TRMM. *J. Climate*, **22**, 414–428.
- DeMott, C. A., and S. A. Rutledge, 1998: The vertical structure of TOGA COARE convection. Part II: Modulating influences and implications for diabatic heating. *J. Atmos. Sci.*, **55**, 2748–2762.
- Emanuel, K. A., 1994: *Atmospheric Convection*. Oxford University Press, 592 pp.
- Fu, R., A. D. Del Genio, and W. B. Rossow, 1994: Influence of ocean surface conditions on atmospheric vertical thermodynamic structure and deep convection. *J. Climate*, **7**, 1092–1108.
- Gill, A. E., 1980: Some simple solutions for heat-induced tropical circulation. *Quart. J. Roy. Meteor. Soc.*, **106**, 447–462.
- Hartmann, D. L., H. H. Hendon, and R. A. Houze, 1984: Some implications of the mesoscale circulations in tropical cloud clusters for large-scale dynamics and climate. *J. Atmos. Sci.*, **41**, 113–121.
- Kalnay, E., and Coauthors, 1996: The NCEP/NCAR 40-Year Reanalysis Project. *Bull. Amer. Meteor. Soc.*, **77**, 437–471.
- Khouider, B., and A. J. Majda, 2006: Multicloud convective parameterizations with crude vertical structure. *Theor. Comput. Fluid Dyn.*, **20** (5–6), 351–375.
- Kuang, Z., 2008: A moisture-stratiform instability for convectively coupled waves. *J. Atmos. Sci.*, **65**, 834–854.
- Kubar, T. L., D. L. Hartmann, and R. Wood, 2007: Radiative and convective driving of tropical high clouds. *J. Climate*, **20**, 5510–5526.
- Lagarias, J., J. Reeds, M. Wright, and P. Wright, 1998: Convergence properties of the Nelder–Mead simplex algorithm in low dimensions. *SIAM J. Optim.*, **9**, 112–147.
- Lindzen, R. S., and S. Nigam, 1987: On the role of sea surface temperature gradients in forcing low-level winds and convergence in the Tropics. *J. Atmos. Sci.*, **44**, 2418–2436.
- Majda, A. J., and M. G. Shefter, 2001: Models for stratiform instability and convectively coupled waves. *J. Atmos. Sci.*, **58**, 1567–1584.
- Mapes, B., 2000: Convective inhibition, subgrid-scale triggering energy, and stratiform instability in a toy tropical model. *J. Atmos. Sci.*, **57**, 1515–1535.
- Matsumoto, T., 1966: Quasi-geostrophic motions in the equatorial area. *J. Meteor. Soc. Japan*, **44**, 25–43.
- Moskowitz, B., and C. Bretherton, 2000: An analysis of frictional feedback on a moist equatorial Kelvin mode. *J. Atmos. Sci.*, **57**, 2188–2206.
- Mote, P. W., and R. Frey, 2006: Variability of clouds and water vapor in low latitudes: View from Moderate Resolution Imaging Spectroradiometer (MODIS). *J. Geophys. Res.*, **111**, D16101, doi:10.1029/2005JD006791.
- Neelin, J. D., 1989: On the interpretation of the Gill model. *J. Atmos. Sci.*, **46**, 2466–2468.
- , and I. M. Held, 1987: Modeling tropical convergence based on the moist static energy budget. *Mon. Wea. Rev.*, **115**, 3–12.
- , and N. Zeng, 2000: A quasi-equilibrium tropical circulation model—formulation. *J. Atmos. Sci.*, **57**, 1741–1766.

- North, G., T. Bell, R. Calahan, and F. Moeng, 1982: Sampling errors in estimation of empirical orthogonal functions. *Mon. Wea. Rev.*, **110**, 699–706.
- Peters, M. E., and C. S. Bretherton, 2005: A simplified model of the Walker circulation with an interactive ocean mixed layer and cloud-radiative feedbacks. *J. Climate*, **18**, 4216–4234.
- , and —, 2006: Structure of tropical variability from a vertical mode perspective. *Theor. Comput. Fluid Dyn.*, **20**, 501–524.
- Ramage, C., 1977: Sea surface temperature and local weather. *Mon. Wea. Rev.*, **105**, 540–544.
- Ramanathan, V., and W. Collins, 1991: Thermodynamic regulation of ocean warming by cirrus clouds deduced from observations of the 1987 El Niño. *Nature*, **351**, 27–32.
- Schumacher, C., R. A. Houze Jr., and I. Kraucunas, 2004: The tropical dynamical response to latent heating estimates derived from the TRMM precipitation radar. *J. Atmos. Sci.*, **61**, 1341–1358.
- Sherwood, S. C., 1999: Convective precursors and predictability in the tropical western Pacific. *Mon. Wea. Rev.*, **127**, 2977–2991.
- Sobel, A. H., 2007: Simple models of ensemble-averaged tropical precipitation and surface wind, given the sea surface temperature. *The Global Circulation of the Atmosphere*, T. Schneider and A. H. Sobel, Eds., Princeton Press, 219–251.
- , and C. S. Bretherton, 2000: Modeling tropical precipitation in a single column. *J. Climate*, **13**, 4378–4392.
- , and J. D. Neelin, 2006: The boundary layer contribution to intertropical convergence zones in the quasi-equilibrium tropical circulation model framework. *Theor. Comput. Fluid Dyn.*, **20** (5–6), 323–350.
- , S. E. Yuter, C. S. Bretherton, and G. N. Kiladis, 2004: Large-scale meteorology and deep convection during TRMM KWAJEX. *Mon. Wea. Rev.*, **132**, 422–444.
- , G. Bellon, and J. Bacmeister, 2007: Multiple equilibria in a single-column model of the tropical atmosphere. *Geophys. Res. Lett.*, **34**, L22804, doi:10.1029/2007GL031320.
- Stevens, B., J. J. Duan, J. C. McWilliams, M. Munnich, and J. D. Neelin, 2002: Entrainment, Rayleigh friction, and boundary layer winds over the tropical Pacific. *J. Climate*, **15**, 30–44.
- Tao, W., E. Smith, R. Adler, Z. Haddad, and A. Hou, 2006: Retrieval of latent heating from TRMM measurements. *Bull. Amer. Meteor. Soc.*, **87**, 1555–1572.
- Trenberth, K. E., D. P. Stepaniak, and J. M. Caron, 2000: The global monsoon as seen through the divergent atmospheric circulation. *J. Climate*, **13**, 3969–3993.
- Uppala, S., and Coauthors, 2005: The ERA-40 Re-Analysis. *Quart. J. Roy. Meteor. Soc.*, **131**, 2961–3012.
- Wang, B., and T. M. Li, 1993: A simple tropical atmosphere model of relevance to short-term climate variations. *J. Atmos. Sci.*, **50**, 260–284.
- Webster, P., 1981: Mechanisms determining the atmospheric response to sea surface temperature anomalies. *J. Atmos. Sci.*, **38**, 554–571.
- Wu, Z. H., D. S. Battisti, and E. S. Sarachik, 2000: Rayleigh friction, Newtonian cooling, and the linear response to steady tropical heating. *J. Atmos. Sci.*, **57**, 1937–1957.
- Yanai, M., S. Esbensen, and J. H. Chu, 1973: Determination of bulk properties of tropical cloud clusters from large-scale heat and moisture budgets. *J. Atmos. Sci.*, **30**, 611–627.
- Yu, J.-Y., C. Chou, and J. D. Neelin, 1998: Estimating the gross moist stability of the tropical atmosphere. *J. Atmos. Sci.*, **55**, 1354–1372.
- Zebiak, S. E., 1982: A simple atmospheric model of relevance to El Niño. *J. Atmos. Sci.*, **39**, 2017–2027.
- , 1986: Atmospheric convergence feedback in a simple-model for El Niño. *Mon. Wea. Rev.*, **114**, 1263–1271.
- Zhang, C., 1993: Large-scale variability of atmospheric deep convection in relation to sea surface temperature in the Tropics. *J. Climate*, **6**, 1898–1913.
- , M. McGauley, and N. A. Bond, 2004a: Shallow meridional circulation in the tropical eastern Pacific. *J. Climate*, **17**, 133–139.
- Zhang, Y., W. B. Rossow, A. A. Lacis, V. Oinas, and M. I. Mishchenko, 2004b: Calculation of radiative fluxes from the surface to top of atmosphere based on ISCCP and other global data sets: Refinements of the radiative transfer model and the input data. *J. Geophys. Res.*, **109**, D19105, doi:10.1029/2003JD004457.
- Zuidema, P., B. Mapes, J. L. Lin, C. Fairall, and G. Wick, 2006: The interaction of clouds and dry air in the eastern tropical Pacific. *J. Climate*, **19**, 4531–4544.